Nuclear polarization and charge moments of ^{208}Pb from muonic x rays

P. Bergem, G. Piller, A. Rueetschi, L. A. Schaller, L. Schellenberg, and H. Schneuwly
Institut de Physique, Université de Fribourg, CH-1700 Fribourg, Switzerland
(Received 13 January 1988)

Muonic transition energies between low-lying states in μ^--^{208}Pb have been measured in a precision experiment using a Compton suppression spectrometer. Nuclear charge parameters and nuclear polarization corrections have been adjusted to the data. In particular, experimental correlations between the nuclear polarization corrections of the lower muonic levels have been established. A set of nuclear charge parameters reproducing all the experimental transition energies can only be obtained by assuming an inversion in magnitude of the nuclear polarization corrections not only for the $2p$ states, but also for the two $3p$ states. Such a result is unexplained by present theoretical models, but corroborates the findings of a recent experiment concerning the $2p$ states in μ^--^{90}Zr. Using our best-fit parameters, a ^{208}Pb rms radius of $\langle r^2\rangle^{1/2}=5.5031(11)$ fm has been obtained.

I. INTRODUCTION

Since the predictions of Wheeler[1] and the first measurement by Fitch and Rainwater,[2] a great deal of progress has been achieved in the field of muonic atoms. Each advance in precision of the measurement of the muonic transition energies raised new questions which required increasingly refined theoretical calculations. Presently, the quantum electrodynamic (QED) corrections, electron screening, relativistic mass, and anomalous magnetic moment corrections are well known or small enough so as not to limit the accuracy with which nuclear charge moments can be deduced from the measured muonic x-ray energies.[3]

The least well-known correction which has to be applied to the muonic atom levels is the nuclear polarization (NP) correction. The calculation of this effect is known to be difficult and imprecise. It demands the use of specific nuclear models and leads to different results depending on the approximations used. Typical quoted theoretical uncertainties range from 10% to 50%. Most of these calculations have been performed for the heavy, doubly-magic nucleus ^{208}Pb,[4–7] but experimental confirmations are largely missing. Rinker and Speth[7] pointed out that there is a significant discrepancy between the calculated and experimental value of the energy splitting of the $2p$ levels in ^{208}Pb. This discrepancy is not due to possible model dependencies of the analysis, based on a Fermi-type charge distribution, as was shown in a more recent study of Yamazaki *et al.*[8] These authors used a model-independent combined analysis of the muonic data of Kessler *et al.*[9] and electron-scattering data.[10] Their study showed that the NP corrections applied to the $2p$ states had to be inversed in magnitude. A similar result was obtained by our group in a recent experiment on muonic ^{90}Zr.[11]

The above discrepancies could point to a yet unobserved resonance excitation process in ^{208}Pb, whereas this possibility seems unlikely in ^{90}Zr. The alternative conclusion could well be a fundamental problem in present theoretical approaches to the nuclear polarization effect.[12] The validity of the above conclusions hinges upon the accuracy of the experimental data. The present work was initiated in order to clarify the experimental situation regarding the muonic data, and perhaps to resolve the discrepancies appearing in the $2p$ splitting of ^{208}Pb. We aimed at precisions of 30 ppm or less for the energies of the transitions involving the lower muonic states. In particular, the transitions to and from the $2s$ state have to be accurately measured because this state is, next to the $1s$ state, the most sensitive to the interior of the nuclear charge distribution in ^{208}Pb. Since these transitions, namely the $2s$-$2p$ and $3p$-$2s$ transitions, are located on top of a large Compton background from more energetic and strongly populated circular transitions, we employed a Compton suppression spectrometer (CSS) in order to obtain the required degree of precision.

The present experiment achieved precisions up to 11 ppm, an overall improvement by a factor of 5 over the Kessler data.[9] Comparison of our data with theory not only confirms the NP discrepancy in the $2p$ states already discussed in Refs. 7 and 8, but exhibits the same kind of discrepancy in the $3p$ states. Preliminary results regarding the present experiment have been communicated at conferences.[13–15]

In the following, Sec. II summarizes the theoretical background concerning muonic binding energies and, specifically, the NP corrections. Section III describes the experimental setup at the superconducting muon channel at Swiss Institute of Nuclear Physics, now Paul Scherrer Institute (SIN). In Sec. IV the data analysis and the calibration method used to determine precise muonic transition energies are discussed. Section V compares the experimental transition energies to the calculated ones, establishes experimentally allowed correlations between the NP corrections of the lower levels, and presents a radial-moment analysis of the data. This section also includes the determination of a self-consistent set of NP corrections to be applied to the different levels. Finally, Sec. VI stresses the discrepancies found for the $2p$ and $3p$ levels and draws the conclusions from these findings.

II. THEORY

In order to obtain information about nuclear charge parameters and energy shifts due to dynamical excita-

tions of the nucleus, we have to compare the measured muonic transition energies with those obtained from calculations. The Dirac equation is numerically solved for the muon in a static central potential with adjustable nuclear charge parameters. The effects of quantum electrodynamics, as well as electron screening and dynamical muon-nucleus interactions, are taken into account by adding to the Dirac equation the corresponding effective potentials in a perturbative way. In the present case of a nucleus with spin zero ground state, the dynamic hyperfine structure effects are negligible.

We write the total Hamiltonian of the muon-nucleus system as

$$\mathcal{H}=H_\mu+H_N+V_0+(V-V_0)=H_0+V_R \ ,$$

where $H_0=H_\mu+H_N+V_0$ contains a muon Hamiltonian H_μ and a nuclear Hamiltonian H_N. The eigenfunctions of this zero-order Hamiltonian H_0 are products of relativistic muonic and nuclear wave functions. H_0 includes a static central potential V_0 representing the average electrostatic potential generated by the charge distribution $\rho(r)$ of the extended nucleus as well as the Uehling potential for the first order vacuum polarization. The muonic part of H_0, H_μ, is assumed to include all corrections not involving nuclear excitations and static nuclear moments. These corrections are the higher orders of the electron-positron vacuum polarization, the $\mu^+\mu^-$ and the hadronic vacuum polarization, the effect of the anomalous magnetic moment, the Lamb shift of first and second order, the relativistic recoil, and the electron screening.[3]

For muonic ^{208}Pb, these different corrections are listed in Table I together with the finite size binding energies. The latter are evaluated using for $V_0(r_\mu)$ a spherically symmetric Fermi-type charge distribution with parameters c and a, namely, the half-density radius and the diffuseness parameter. The parameters used for calculating the values of Table I have already been adjusted to the experimental data, as will be discussed in Sec. V.

The second term of the total Hamiltonian $\mathcal{H}$, V_R, describes the dynamical muon-nucleus interaction, resulting in additional shifts of the muonic levels. These shifts are known as (NP) corrections. For a qualitative understanding of these effects one may refer to the simple picture of a negative probe, the muon, penetrating the positive charge distribution of the nucleus. Hence, the Coulomb repulsion is reduced, the nuclear charge shrinks, and, consequently, the binding energy of the total system increases. A realistic approach of the problem must take into account that each different muonic wave function induces different nuclear deformations of different multipolarities and strengths. The difference between the static nuclear charge distribution and the actual one is treated by the residual muon-nuclear interaction potential $V_R=V-V_0$ which changes the muonic and nuclear states by admixing or virtually exciting other states. The de-excitation of these nuclear states to the ground state transfers energy back to the muon, and hence does not result in real final state excitations of the nucleus. As a consequence, the muonic cascade proceeds between muonic atom levels which are displaced from the positions they would have occupied for a static nuclear charge.[7]

In first order, the dynamical shift of the binding energy of the ith muonic state is zero. The second-order shift however, where the off-diagonal matrix elements involve different muonic and nuclear states, does not vanish. It is calculated as

$$\Delta E_{\rm NP}=\sum_{i\neq j}\frac{|\langle j\,|\,V_R\,|\,i\rangle|^2}{E_i-E_j} \ ,$$

where $|\,i\rangle$ is the muon state in question, coupled to the nuclear ground state, and the $\langle j\,|$ states represent the entire spectrum of all other muonic and excited nuclear states. The lack of knowledge of the complete spectrum

TABLE I. Corrections to muonic binding energies in ^{208}Pb (keV). Note: A positive correction means an increase in binding energy.

State	Finite size binding energy a	Vacuum polarization (VP) b	c	d	e	total	Lamb shift f	Other corrections g
$1s_{1/2}$	10 592.399	67.249	0.553	−0.492	0.410	67.720	−3.814	0.385
$2s_{1/2}$	3600.013	19.412	0.149	−0.244	0.071	19.387	−0.792	0.111
$2p_{1/2}$	4814.776	32.470	0.251	−0.348	0.074	32.447	−0.650	0.120
$2p_{3/2}$	4630.089	29.919	0.229	−0.335	0.056	29.869	−0.911	0.106
$3p_{1/2}$	2139.335	10.810	0.082	−0.160	0.023	10.708	−0.226	0.082
$3p_{3/2}$	2091.890	10.277	0.077	−0.160	0.019	10.213	−0.301	0.080
$3d_{3/2}$	2173.037	10.563	0.075	−0.186	0.002	10.454	0.099	0.051
$3d_{5/2}$	2130.158	9.899	0.070	−0.180	0.001	9.791	−0.098	0.052

[a]Including first order VP. The best fit parameters c and a of Table VIII were used in these calculations.
[b]First order VP (approximative values).
[c]Second order VP.
[d]VP orders ≥ 3.
[e]Muonic and hadronic VP.
[f]First- and second-order vertex corrections, including anomalous magnetic moment.
[g]Relativistic recoil and electron screening corrections.

TABLE II. Theoretical nuclear polarization corrections in ^{208}Pb.

Energy (MeV)	I^π	$B(E\lambda)\uparrow$ ($e^2b^{2\lambda}$)	$1s_{1/2}$ (eV)	$2s_{1/2}$ (eV)	$2p_{1/2}$ (eV)	$2p_{3/2}$ (eV)	$3p_{1/2}$ (eV)	$3p_{3/2}$ (eV)	$3d_{3/2}$ (eV)	$3d_{5/2}$ (eV)
2.615	3^-	0.612	135	12	90	84	26	26	111	−63
4.085	2^+	0.318	198	20	182	180	76	84	6	4
4.324	4^+	0.155	14	1	8	7	2	2	1	1
4.842	1^-	0.001 56	7	1	−9	−8	0	0	1	1
5.240	3^-	0.130	27	2	16	15	5	5	2	2
5.293	1^-	0.002 04	9	2	−27	−19	0	−1	1	1
5.512	1^-	0.003 80	16	3	−90	−53	−1	−1	1	1
5.946	1^-	0.000 07	0	0	3	−30	0	0	0	0
6.193	2^+	0.050 5	29	3	22	21	7	7	0	0
6.262	1^-	0.000 24	1	0	3	5	0	0	0	0
6.312	1^-	0.000 22	1	0	3	4	0	0	0	0
6.363	1^-	0.000 14	1	0	2	2	0	0	0	0
6.721	1^-	0.000 75	3	1	6	7	0	−1	0	0
7.064	1^-	0.001 56	6	1	9	11	−1	−1	0	0
7.083	1^-	0.000 75	3	1	4	5	−1	−1	0	0
7.332	1^-	0.002 04	8	1	10	11	−2	−2	0	0
Total low-lying states			458	48	233	242	111	117	123	−53
13.5	0^+	0.047 872	906	315	64	38	24	15	1	0
22.8	0^+	0.043 658	546	147	43	26	15	10	0	0
13.7	1^-	0.537 672	1454	221	786	738	255	258	66	54
10.6	2^+	0.761 038	375	37	237	222	67	68	33	30
21.9	2^+	0.566 709	207	21	108	99	29	29	8	7
18.6	3^-	0.497 596	77	7	40	36	11	11	3	2
33.1	3^-	0.429 112	53	5	25	23	7	7	2	1
	>3[a]		176	15	80	71	21	21	4	4
Total high-lying states			3794	768	1383	1253	429	419	117	98
Total			4252	816	1616	1495	540	536	240	45

[a]Values from Ref. 7. Positive NP values mean that the respective binding energies are increased.

of nuclear excited states, both discrete (low-lying) and continuous (high-lying) ones, requires the use of specific nuclear models.[16]

The contributions of the high-lying continuous nuclear states are evaluated by normalizing the transition charge densities with energy-weighted sum rules and by concentrating the reduced transition probabilities $B(E\lambda)\uparrow$ in single giant resonances whose energies are derived from an empirical expression.[3,7] The contributions from low-lying discrete nuclear states are calculated using the experimental transition probabilities $B(E\lambda)\uparrow$.[17]

The computer codes MUON and MUON2 (Ref. 18) were used to calculate the NP contributions for the muonic $1s$, $2s$, $2p_{1/2}$, $2p_{3/2}$, $3p_{1/2}$, $3p_{3/2}$, $3d_{3/2}$, and $3d_{5/2}$ states in ^{208}Pb. Table II summarizes the results of these calculations.

III. EXPERIMENT

A. Beam and target

The experiment has been performed during three runs at the superconducting μE1 channel of the SIN accelerator at Villigen, Switzerland. The primary proton beam had intensities between 110 and 120μA. The magnetically selected momentum of muons from backward decaying pions was 125 MeV/c. After passing through a beryllium degrader, the muons were stopped in targets of ^{208}PbO or ^{208}Pb$(NO_3)_2$. Table III gives the target masses, dimensions, and isotopic compositions. Typical stopping rates in the 1.74 g/cm^2 thick target, as measured by a $123\bar{4}$ coincidence in a scintillation counter telescope (Fig. 1), were $10^6\mu^-$/s, corresponding to 20% of the incoming muons.

TABLE III. Target masses and isotopic compositions.

Compound	Mass (g)	Surface (cm^2)	Thickness (g/cm^2)	Amount of Pb (g)	Isotopic abundance (%) 208 207 206 204
PbO	15	4×5	0.75	13.9	98.69/1.03/0.28/0.05
$Pb(NO_3)_2$	20	4×5	1.	12.5	99.47/0.39/0.14/0.007
Total	35	4×5	1.75	26.4	99.14/0.66/0.20/0.03

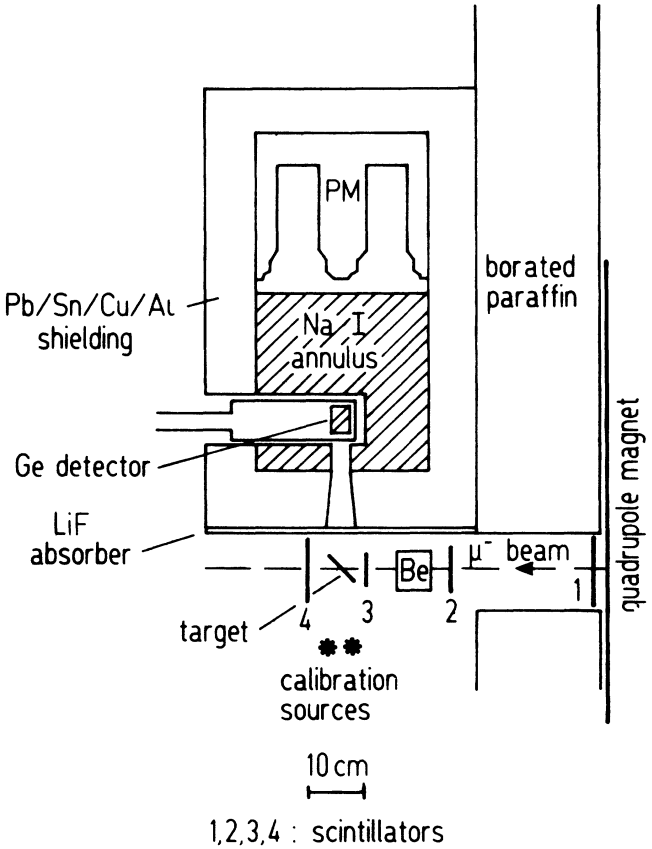

FIG. 1. Target area including the Compton suppression spectrometer (CSS).

B. Detectors

The muonic x rays and γ rays from the target and the calibration sources were detected by Ge detectors. In the first run, covering the energy range up to 1600 keV, including the $2s$-$2p$ and $3p$-$2s$ muonic transitions in ^{208}Pb [Fig. 2(a)], a 66 cm^3 high-purity, intrinsic n-type Ge detector was used as part of a Compton suppression spectrometer (CSS). At a counting rate of 5000/s under in-beam conditions, the resolution (FWHM) of this detector was 2.0 keV at 1332 keV, and its line shape was almost Gaussian. The CSS consisted of the above Ge detector surrounded in an asymmetrical way by a NaI(Tl) annulus of diameter 22 cm and length 29 cm. These dimensions had been chosen in order to yield a 90% absorption of Compton-scattered γ rays up to 3 MeV.[19] Under in-beam conditions, and in the energy region of interest (900–1500 keV), an average background suppression factor of 4 was achieved. Figure 2(b) shows the weakly populated $2s$-$2p_{1/2}$ transition as measured with and without the CSS. The weak $2s$-$2p$ and $3p$-$2s$ transitions are on top of a large Compton background from higher-lying transitions between strongly populated circular orbits ($2p$-$1s$, $3d$-$2p$). Without Compton suppression it would not have been possible to obtain the required energy precision for these transitions which are crucial in the following search for nuclear parameters.

In the second run, covering the energy range up to 3500 keV, including the muonic $3d$-$2p$ transitions, we employed a 50 cm^3 coaxial Ge(Li) detector with a resolution (FWHM) of 2.5 keV at 1332 keV under in-beam conditions at a counting rate of 7000/s.

The third run covered the energy range up to 6500 keV, including the muonic $2p$-$1s$ transitions. The 66 cm^3 intrinsic Ge detector was used without its anti-Compton shield. Its resolution was 5.0 keV at 6129 keV (^{16}O* line) under in-beam conditions at counting rates of 6000/s.

C. Setup and shielding

In general, the experimental setup was similar to earlier runs.[20–22] Special care was taken in the run with the CSS in order to reduce the background due to beam and secondary radiation sources. Since high background loads in the NaI(Tl) annulus reduce the number of accepted photopeak events in the central detector by accidental coincidences, the CSS was shielded by a

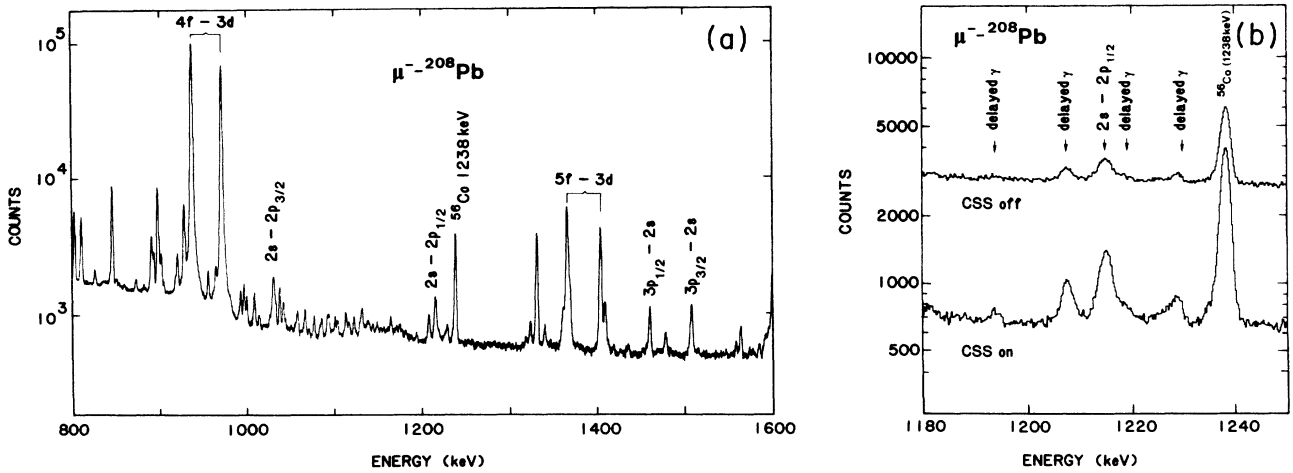

FIG. 2. Muonic x-ray spectra; (a) Low energy region taken with the CSS. (b) Close up of the $2s$-$2p_{1/2}$ region taken with and without the CSS.

sandwich (Pb-Sn-Cu-Al) absorber. In addition, borated paraffin and a sheet of cadmium protected the detector against scattered neutrons. The part of the annulus facing the target was covered by a layer of LiF in order to reduce the neutron flux due to nuclear muon capture in the target. Figure 1 shows the CSS setup in the target area.

D. Calibration sources

Gamma rays from calibration sources (^{16}N, ^{56}Co, ^{192}Ir) were recorded simultaneously with the muonic x rays. Regarding the ^{16}N, we made use of the ^{16}O(n,p)^{16}N reaction, which takes place in the cooling water around the thick target area E of SIN. A sample of this radioactive water was piped towards our experimental station in the μE1 area in less than 10 s. Hence, by way of the 7.2 s β^- activity of ^{16}N, there remains enough population of the 6129 keV level of ^{16}O. The energy of the corresponding γ ray to the ground state has recently been measured with high precision.[23,24] In order to avoid geometrical effects in the Ge detectors, the sources were placed close to the target. Hence, the calibration γ rays had a similar direction as the incoming muonic x rays without encountering any material on their way to the detector.

Besides the on-line calibration, we also recorded calibration spectra off-line at each run. These spectra were used to determine the nonlinearity of our detecting system. Table IV gives the list of calibration sources with their principal lines and errors.[23–25]

TABLE IV. Calibration sources and their γ-ray energies used for calibration and detector system nonlinearity.

Source	References	Energies (keV)	
^{56}Co	25	846.764(6)	1037.844(4)
		1175.099(8)	1238.287(6)
		1360.206(6)	1771.350(15)
		1963.714(12)	2015.179(11)
		2034.759(11)	2598.460(10)
		3009.596(17)	3201.954(14)
		3253.417(14)	3272.998(14)
		3451.154(13)	
^{110}Ag^m	25	446.811(3)	620.360(3)
		657.762(2)	677.623(2)
		687.015(3)	706.682(3)
		744.277(3)	763.944(3)
		818.031(4)	884.685(3)
		937.493(4)	1384.300(4)
		1475.788(6)	1505.040(5)
		1562.302(5)	
^{192}Ir	25	316.508 0(8)	416.471 9(12)
		468.071 5(12)	484.577 9(13)
		588.585 1(16)	604.414 6(16)
		612.465 7(16)	884.542 3(20)
^{207}Bi		569.702(2)	1063.662(4)
^{16}N	23	6129.142(32)	
	24	6129.119(40)	
		weighted mean	6129.133(25)

E. Data acquisition

The electronic setup was similar to the one used in former runs (Refs. 20–22). The recorded 8k spectra can be divided into the following three categories.

(a) "Prompt" spectra, recorded in prompt coincidence with a stopped muon, the widths of the time windows ranging from 16 to 30 ns. These relatively small widths ensured that the spectra contained essentially only x rays from the muonic cascade.

(b) "Delayed" spectra, recorded within 30–200 ns after a muon stop. These spectra preferentially contained delayed γ rays, resulting from nuclear muon capture in the target.

(c) "Calibration" spectra, recorded when the counter telescope indicated that an incoming muon was not stopped in the target ($\overline{1234}$). In this way, the beam load could be closely reproduced and the calibration events were measured under almost the same experimental conditions as the muonic events. The main purpose of these spectra was the determination of the line shapes of our detecting system. This technique has been carefully tested in previous experiments.[20]

It should be noted that the calibration lines are also present in the prompt, and, in particular, the delayed spectra due to accidental feedthrough. These lines have been used for the final energy calibration (see Sec. IV).

Finally, we recorded in each run a spectrum using a beryllium dummy target instead of the lead target, without calibration sources. The purpose of these measurements was to ensure that no background lines from the environment were present underneath the muonic transitions or calibration lines.

Since the uncertainty of the line positions depends linearly on the line widths, energy resolution and line shape were optimized for the most important transition in each spectrum. In order to avoid broadening of the lines by long term electronic or temperature drifts of the detecting system, histograms were stored on tape every 5–8 h.

In order to obtain good statistics, a large number of 8k spectra had to be recorded on tape for each energy region of interest. Each histogram was analyzed in order to eliminate those showing line broadenings exceeding 5% due to electronic or temperature-induced shifts. In this way roughly 10% of the histograms were discarded. In addition, every histogram was checked for two strong calibration lines situated at the extremes of the respective spectra. If necessary, the channel contents were shifted in order to match the positions of these lines in a reference histogram before adding up the histograms of the whole run. This procedure eliminates the small displacements of the peaks due to long-term drifts in the analog-to-digital converter (ADC) baseline and the linear amplifier gain setting.

IV. ENERGY CALIBRATION AND TRANSITION ENERGIES

A. General considerations

In the first step of the analysis, the delayed calibration and Be-dummy-target spectra were checked for possible

contaminants underneath the calibration γ- and muonic x-ray peaks. In such a way, a set of clean, isolated calibration lines could be selected. The MYFIT (Ref. 26) fitting routine using a Gaussian function convoluted with a Lorentzian and exponential tails was then applied to this set of lines in order to determine the experimental line shape. Firstly, average tail parameters were deduced from the fits. Using these mean parameters, the Gaussian line widths (FWHM) and their dependence on energy were obtained. Nonresolved doublets could easily be detected by comparing their widths to the expected single peak widths.

Finally, all the calibration, delayed and muonic lines were fitted using the above set of parameters with the Lorentzian line widths being fixed at the values of the calculated natural line widths.

Isotopic impurities of the lead target (see Table III) were taken into account by including in the fits the lines of ^{206}Pb and ^{207}Pb with appropriate relative intensities. The positions of these lines with respect to the ^{208}Pb line were calculated from published isotope shifts of earlier work.[9]

B. Nonlinearity, calibration, and systematic errors

The nonlinearity corrections of the detecting system were determined from ^{56}Co, ^{110}Ag^{m}, ^{192}Ir, and ^{207}Bi sources. These calibrations were made on-line in the second run ($3d$-$2p$). In the first ($2s$-$2p$) and third ($2p$-$1s$) runs, the corresponding calibration spectra were taken off-line. Different amplifier gain settings were used in the third run, due to lack of calibration sources in the range from 3500 to 6000 keV. All spectra showed essentially the same nonlinearity behavior. A smooth curve was fitted to the nonlinearity data of each run, and the obtained corrections were applied to the prompt and delayed spectra.

The absolute energy calibration of the muonic lines was obtained using the positions of the ^{16}N and ^{56}Co lines (see Table IV) in the delayed spectra. This procedure guarantees experimental conditions as close as possible to those encountered in the prompt spectra. Nevertheless, a shift between the two spectra might still occur due to the different widths of the timing windows, inducing different instantaneous detector loads. We therefore compared the positions of the most intense γ lines in both spectra and consequently corrected the positions of the x-ray lines to be calibrated. In the $2s$-$2p$ spectrum, this correction amounted to 6(1) eV, in the $3d$-$2p$ spectrum to $-1(3)$ eV, and in the $2p$-$1s$ spectrum to 50(40) eV.

C. Transition energies

Table V shows the transition energies which are obtained by adding the recoil energy of the nucleus to the measured muonic x-ray energies. The quoted errors are total errors including statistical, calibration, and systematic uncertainties.

The most precise previous measurements of the K, L, and M transition energies in muonic lead are the ones of Kessler *et al.*[9] and Hoehn and Shera,[27] whose results are also listed in Table V. Our errors are typically 4–6 times smaller than those of the older measurement of Kessler and comparable to those of Hoehn and Shera for the cir-

TABLE V. Experimental muonic transition energies (keV) in ^{208}Pb (recoil corrected).

Transition	Kessler (Ref. 9)	Hoehn (Ref. 27)	This experiment
$2p_{3/2}$-$1s_{1/2}$	5 962.770(420)		5 962.854(90)
$2p_{1/2}$-$1s_{1/2}$	5 777.910(400)		5 778.058(100)
$3d_{3/2}$-$2p_{1/2}$	2 642.110(60)	2642.292(23)	2 642.332(30)
$3d_{5/2}$-$2p_{3/2}$	2 500.330(60)	2500.580(28)	2 500.590(30)
$3d_{3/2}$-$2p_{3/2}$	2 457.200(200)		2 457.569(70)
$3p_{3/2}$-$2s_{1/2}$	1 507.480(260)		1 507.754(50)
$3p_{1/2}$-$2s_{1/2}$			1 460.558(32)
$2s_{1/2}$-$2p_{1/2}$	1 215.430(260)		1 215.330(30)
$2s_{1/2}$-$2p_{3/2}$	1 030.440(170)		1 030.543(27)
$5f_{5/2}$-$3d_{3/2}$	1 404.740(80)		1 404.659(20)
$5f_{7/2}$-$3d_{5/2}$	1 366.520(80)		1 366.347(19)
$5f_{5/2}$-$3d_{5/2}$			1 361.748(250)
$4f_{5/2}$-$3d_{3/2}$	971.850(60)	971.971(16)	971.974(17)
$4f_{7/2}$-$3d_{5/2}$	937.980(60)	938.113(13)	938.096(18)
$4f_{5/2}$-$3d_{5/2}$			928.883(14)
$4d_{3/2}$-$3p_{1/2}$			920.959(28)
$4d_{5/2}$-$3p_{3/2}$			891.383(22)
$4d_{3/2}$-$3p_{3/2}$			873.761(63)

TABLE VI. Fine structure level splittings in muonic ^{208}Pb (keV).

Splitting	Kessler (Ref. 9)	Hoehn (Ref. 27)	This experiment
$\Delta(2p)$ from $2p$-$1s$	184.830(100)		184.796(40)
from $2s$-$2p$	184.990(310)		184.787(42)
from $3d$-$2p$	184.890(250)		184.763(70)
weighted mean	184.851(90)		184.788(27)
$\Delta(3p)$ from $3p$-$2s$			47.196(60)
from $4d$-$3p$			47.198(69)
weighted mean			47.197(45)
$\Delta(3d)$ from $3d$-$2p$	43.130(180)		43.021(70)
from $4f$-$3d$	[a]43.070(30)		43.045(26)
from $5f$-$3d$	[a]42.950(100)		42.911(250)
weighted mean	43.060(30)		43.041(24)
$\Delta(4d)$			17.622(67)
$\Delta(4f)$			9.187(26)
$\Delta(5f)$			4.599(250)
$\Delta(2p)$-$\Delta(3d)$	141.770(60)	141.710(36)	141.742(42)
$\Delta(3p)$-$\Delta(4d)$			29.576(37)
$\Delta(3d)$-$\Delta(4f)$	33.870(80)	33.858(21)	33.858(25)
$\Delta(3d)$-$\Delta(5f)$			38.312(28)

[a] f-splitting fixed at theoretical value.

cular L and M lines.

Table VI gives a list of internal consistency checks provided by the level splittings as calculated from different transitions. There is particularly good internal agreement in the $2p$ and $3p$ splittings. Also listed are some intradoublet energy differences and their values from earlier work.

Comparison with the Kessler data reveals systematically higher energies in our work, whereas the splittings are in agreement. The fact that Kessler *et al.* employed older calibration energy standards does not alter the situation, as an analysis of our data with the older standards shows.

V. RESULTS

A. General considerations

In this Sec. V, we utilize the muonic-atom transition energies in order to extract the nuclear charge distribution parameters and the nuclear polarization corrections of the low-lying muonic levels.

In a first step, we take the theoretical NP corrections at face value and try to fit a two-parameter Fermi-type charge distribution to the experimental data. The difficulties arising from this procedure lead to a closer study of the correlations between the NP corrections of the different levels. The final result will be a set of NP corrections and nuclear charge parameters which fit the experimental transition energies.

The main difficulty in analyzing the NP effect lies in the fact that the static nuclear charge distribution is not known beforehand and that a simultaneous fit of NP and charge parameters does not separate the static and dynamical effects. Regarding the low-lying muonic levels sensitive to the nuclear charge distribution, we have precisely measured nine transition energies, namely, $2p_{1/2}$-$1s$, $2p_{3/2}$-$1s$, $3d_{3/2}$-$2p_{1/2}$, $3d_{3/2}$-$2p_{3/2}$, $3d_{5/2}$-$2p_{3/2}$, $3p_{1/2}$-$2s$, $3p_{3/2}$-$2s$, $2s$-$2p_{3/2}$, and $2s$-$2p_{1/2}$, involving eight levels ($1s$, $2s$, $2p_{1/2}$, $2p_{3/2}$, $3p_{1/2}$, $3p_{3/2}$, $3d_{3/2}$, and $3d_{5/2}$) sensitive to static and dynamic effects. The eight NP parameters of these levels have to be determined in addition to the two charge parameters (c,a) of a Fermi charge distribution. The specific form of the chosen charge distribution is not the determining factor in the analysis since the muonic transition energies are sensitive to certain nuclear charge moments only as will be discussed below.

B. Analysis using the theoretical NP values

In a first step, we compared the measured transition energies to those calculated using theoretical NP corrections. The latter were evaluated employing the program MUON2,[18] where the considerations of Sec. II were applied with the most recent nuclear transition data of Ref. 17 included. The comparison of transition energies was performed using the computer code XRAY2,[18] with c and a of the Fermi charge distribution as free parameters. The result is shown in column 5 of Table VII. The fit to the data is very poor ($\chi^2/\mathrm{DF}=187$), differences of more than ten standard deviations showing up. If we attribute this bad fit to a wrong NP correction in the most sensitive s levels, and if we treat $C_{\mathrm{NP},1s}$ and $C_{\mathrm{NP},2s}$ as free parameters, the fit does not drastically improve ($\chi^2/\mathrm{DF}=43$).

In order to gain insight into which levels are responsi-

TABLE VII. Calculated and experimental transition energies and their associated equivalent radii, assuming theoretical NP values.

Transition	C_z (fm/eV)	k	Experimental energy E (keV)	Calculated energy E^0 (keV)	E-E^0 (eV)	Equivalent radii Calc. $R^0_{k,\alpha}$ [c] (fm)	Equivalent radii Expt. $R_{k,\alpha}$ [d] (fm)
$2s_{1/2}$-$2p_{1/2}$	−2.136−5	1.145 6	1 215.330(30)	1 215.543	−213	6.877 6	6.882 1(6)
$2s_{1/2}$-$2p_{3/2}$	−1.268−5	1.399 3	1 030.543(27)	1 030.431	112	6.938 4	6.937 0(3)
$3p_{1/2}$-$2s_{1/2}$	8.547−6	1.847 4	1 460.558(32)	1 460.506	52	6.995 6	6.996 0(3)
$3p_{3/2}$-$2s_{1/2}$	7.909−6	1.871 5	1 507.754(50)	1 508.037	−283	6.998 0	6.995 8(4)
$2p_{1/2}$-$1s_{1/2}$	1.478−6	2.242 9	5 778.058(100)	5 777.831	227	7.031 6	7.031 9(1)
$2p_{3/2}$-$1s_{1/2}$	1.406−6	2.255 9	5 962.854(90)	5 962.943	−89	7.032 1	7.032 0(1)
$3p_{3/2}$-$1s_{1/2}$	1.313−6	2.339 3	8 501.151(100)[b]	8 501.411	−260	7.039 5	7.039 1(1)
$3p_{1/2}$-$1s_{1/2}$	1.330−6	2.340 7	8 453.946(105)[b]	8 453.879	67	7.039 6	7.039 7(1)
$3d_{5/2}$-$1s_{1/2}$	1.271−6	2.374 0	8 463.444(95)[b]	8 463.328	116	7.042 3	7.042 4(1)
$2s_{1/2}$-$1s_{1/2}$	1.573−6	2.461 0	6 993.393(100)[b]	6 993.374	19	7.049 2	7.049 2(2)
$\Delta(2p)$	2.921−5	2.532 9	184.788(27)[a]	185.112	−324	7.054 8	7.045 3(8)
$\Delta(3p)$	1.048−4	3.232 9	47.197(45)[a]	47.531	−334	7.106 3	7.071 0(47)
$3d_{3/2}$-$2p_{1/2}$	9.128−6	3.478 1	2 642.332(30)	2 642.478	−146	7.123 5	7.122 2(3)
$3d_{3/2}$-$2p_{3/2}$	1.329−5	4.045 4	2 457.569(70)	2 457.366	203	7.162 7	7.165 4(9)
$3d_{5/2}$-$2p_{3/2}$	1.318−5	4.069 9	2 500.590(30)	2 500.385	205	7.164 3	7.167 0(4)

[a]Adopted value from Table VI, Sec. III.
[b]Derived from triangular sums of other measured transition energies.
[c]Calculated from the fit with theoretical NP values, $c=6.644\,68(47)$ fm, $a=0.524\,88(31)$ fm, $\alpha=0.1415$ fm^{-1}.
[d]$R_{k,\alpha}=R^0_{k,\alpha}+C_z(E-E^0)$, errors correspond to transition energy errors.

ble for the poor fit, we performed a radial moment analysis. This type of analysis was introduced by Ford and Wills[28] and Barrett,[29] who related each muonic transition energy to a different generalized moment of the charge distribution. The method is based on the fact that the difference in potentials generated by the muon in the initial and the final state can be well approximated by the expression

$$V_i(r)-V_f(r)=A+Br^k e^{-\alpha r},$$

where the parameter k is a characteristic quantity for each transition, and the factor $e^{-\alpha r}$ is a correction factor with the parameter α usually kept constant for all transitions within the same muonic atom. For a spherically symmetric nuclear charge, each transition energy is then proportional to the "Barrett moment"

$$\langle r^k e^{-\alpha r}\rangle=\int_0^\infty \rho(r) r^k e^{-\alpha r} 4\pi r^2 dr = \frac{3}{R_{k,\alpha}}\int_0^{R_{k,\alpha}} r^k e^{-\alpha r} r^2 dr .$$

The "Barrett equivalent radius" $R_{k,\alpha}$ is the radius of a uniformly charged sphere yielding the same Barrett moment as the actual charge distribution.

In the present work, the parameters k and α were adjusted using the programs ALPHAKA (Ref. 30) and BARRETT (Ref. 18) until the Barrett moment precisely corresponded to the respective transition energy. In these fits, all corrections beyond finite nuclear size, including the theoretical NP corrections as listed in Table II, were included. The equivalent radii $R_{k,\alpha}$ obtained in this way are model independent, in the sense that the form of the nuclear charge distribution used to calculate the respective nuclear moment affects the numerical value of this moment much less than the experimental errors.[31]

Table VII shows the experimental (E) and the calculated (E^0) transition energies and the corresponding equivalent radii. The radii $R^0_{k,\alpha}$ are calculated employing the theoretical NP corrections and the corresponding charge parameters. The "experimental equivalent radii" $R_{k,\alpha}$ are obtained from the $R^0_{k,\alpha}$ using the relation

$$R_{k,\alpha}=R^0_{k,\alpha}+C_z(E-E^0),$$

where C_z is the sensitivity of the transition energy to the equivalent radius. The parameter α has been kept constant at the predetermined value $\alpha=0.1415$ fm^{-1}. The sensitivities C_z and the exponent k for each transition are also listed in Table VII.

Figure 3(a) displays the results of the above procedure in the form of a smooth curve of the calculated values $R^0_{k,\alpha}$ vs k. The experimentally measured moments are represented by dots. Their errors, corresponding to the experimental energy errors of the associated transitions, are in each case smaller than the dots. The most striking feature of this representation is the discrepancy of the moments associated to the $2p$ and $3p$ splittings with respect to the calculated values. This fact corroborates the conclusions of Yamazaki *et al.*,[8] who found that the main source of the discrepancy between "measured" and theoretical NP corrections were the relative values of the two $2p$ states. Their analysis could not include the $3p$ splitting, which deviates in our analysis by more than five standard deviations from the calculated $R^0_{k,\alpha}$ curve. In the case of the $2p$ splitting, the discrepancy amounts to eight standard deviations.

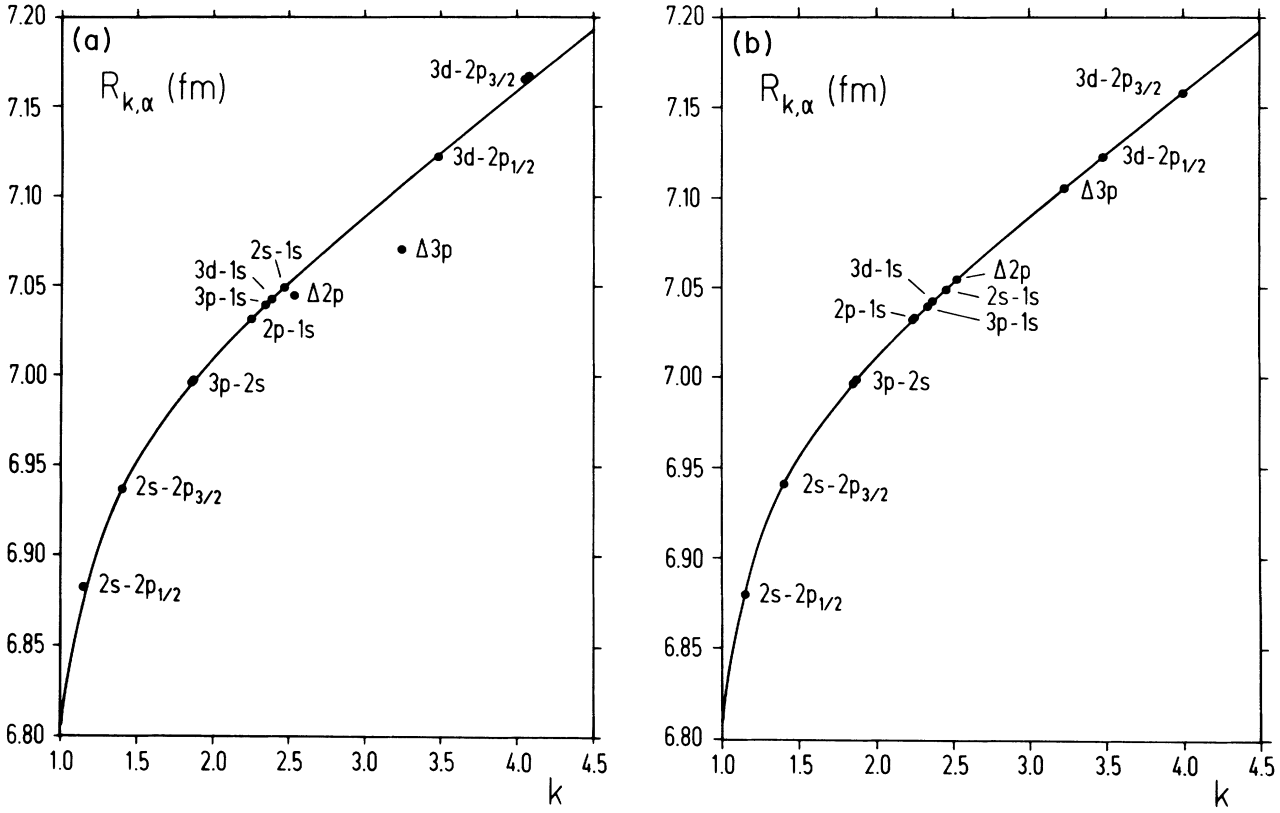

FIG. 3. (a) Plot of the calculated and experimental equivalent radii assuming theoretical NP values. (b) Plot of the calculated and experimental equivalent radii using the best-fit NP values and nuclear charge parameters.

C. Experimental correlations between NP corrections

In order to understand the inconsistencies found in the above analysis, we studied the correlations between the NP corrections of the low-lying muonic levels.

Preliminary fits showed that up to six parameters could be varied together, still ensuring convergence when fitting the calculated transition energies to the measured ones. In order to determine the experimentally allowed values for the NP shifts of the $2s$, the two $2p$, and the two $3p$ states, we varied these quantities together with the half-density radius c of the Fermi charge distribution. The diffuseness parameter was taken from electron scattering experiments[32] as $a=0.5203(40)$ fm, whereas the $C_{\mathrm{NP},3d}$ values were taken from theory (Table II). This procedure was repeated for different fixed $C_{\mathrm{NP},1s}$ values. The NP corrections corresponding to each χ^2-minimum for a given $C_{\mathrm{NP},1s}$ value were then plotted as a function of $C_{\mathrm{NP},1s}$. The results are shown in Figs. 4(a)–4(c) for $C_{\mathrm{NP},2s}$, and for the two differences $\Delta C_{\mathrm{NP},2p}=C_{\mathrm{NP},2p_{1/2}}-C_{\mathrm{NP},2p_{3/2}}$, and $\Delta C_{\mathrm{NP},3p}=C_{\mathrm{NP},3p_{1/2}}-C_{\mathrm{NP},3p_{3/2}}$. The shaded areas in the graphs correspond to uncertainties of ± 105 eV for $C_{\mathrm{NP},2s}$, of ± 54 eV for the difference $\Delta C_{\mathrm{NP},2p}$, and of ± 103 eV for the $\Delta C_{\mathrm{NP},3p}$ difference. These uncertainties have been evaluated by varying the diffuseness parameter a within its error of ± 0.004 fm and by assuming a 30% error on the theoretical $C_{\mathrm{NP},3d}$ values, in addition to the statistical fit errors. Also shown in Figs. 4(a)–4(c) are the results of the theoretical calculations based on Rinker and Speth[7] (see Sec. II, Table II).

Figure 4(a) shows essentially a one-to-one relationship between the $1s$ and the $2s$ nuclear polarizations. Such a constant ratio is predicted by theory, due to the predominance of the giant monopole resonance in spherically symmetric states with angular momentum zero.[3,7] The theoretical calculations are consistent with the experimental results of the two s states. However, there is a discrepancy when comparing the s states and the p states. Theory predicts positive differences in the NP of these states, namely $+121$ eV for the $2p$ states and $+4$ eV for the $3p$ states. At the theoretical value for $C_{\mathrm{NP},1s}$, 4252 eV, the experimental values for these differences are $-324(54)$ eV for the $2p$ states [Fig. 4(b)] and $-334(103)$ eV for the $3p$ states [Fig. 4(c)]. The discrepancy between theoretical and experimentally allowed values amounts to 6.0 and 3.2 standard deviations, respectively, assuming the theoretical $C_{\mathrm{NP},1s}$ value to be correct.

Agreement between theory and experiment concerning the differences in the $2p$ and $3p$ states requires NP values of the $1s$ state of more than 12 and 31 keV, respectively. Such large values are extremely unlikely considering the theoretical values and their estimated errors.[7] In addition, we analyzed the more recent elastic electron scattering data[33] in order to obtain an additional constraint on the $C_{\mathrm{NP},1s}$ value. Taking all corrections beyond finite size, excepting nuclear polarization into account, we employed the parameters a_ν of the Fourier-Bessel charge

distribution from the (e,e) measurement to calculate the muonic binding energies. The difference between the calculated transition energies and the measured ones can then be interpreted as experimentally determined nuclear polarization corrections. Specifically, fixing the $C_{\mathrm{NP},2p}$ at their theoretical values, the differences between the calculated and measured $2p$-$1s$ transitions yields the $C_{\mathrm{NP},1s}$ correction. In order to evaluate the error on this value, the equivalent radii $R_{k,\alpha}$ and their errors $dR_{k,\alpha}$ were calculated from the Fourier-Bessel charge distribution coefficients a_ν and their uncertainties da_ν.[34] These errors were then transformed into energy errors by using the sensitivities C_z

$$dE = C_z^{-1} \cdot dR_{k,\alpha} \ .$$

With the values for α, k, and C_z given in Table VII, the analysis yielded $C_{\mathrm{NP},1s} = 8.8(5.1)$ keV, a result which is not in contradiction with theory. A change of the order of 300 eV in the $2p$ nuclear polarizations does not significantly alter this result.

The above findings are at the root of the difficulties encountered if we try to follow an older line of analysis, fitting the $C_{\mathrm{NP},1s}$ and $C_{\mathrm{NP},2s}$ corrections together with the two parameters c and a of a Fermi charge distribution, with the $C_{\mathrm{NP},2p}$ and $C_{\mathrm{NP},3p}$ values taken from theory ($\chi^2/\mathrm{DF}=43$). Entering the $C_{\mathrm{NP},2p}$ values as free parameters, the fit results in $C_{\mathrm{NP},2p}$ corrections reversed in magnitude. However, the fit remains rather poor ($\chi^2/\mathrm{DF}=29$), due to the bad adaptation to the $3p$-$2s$ transitions which are off by 150 eV or five standard deviations.

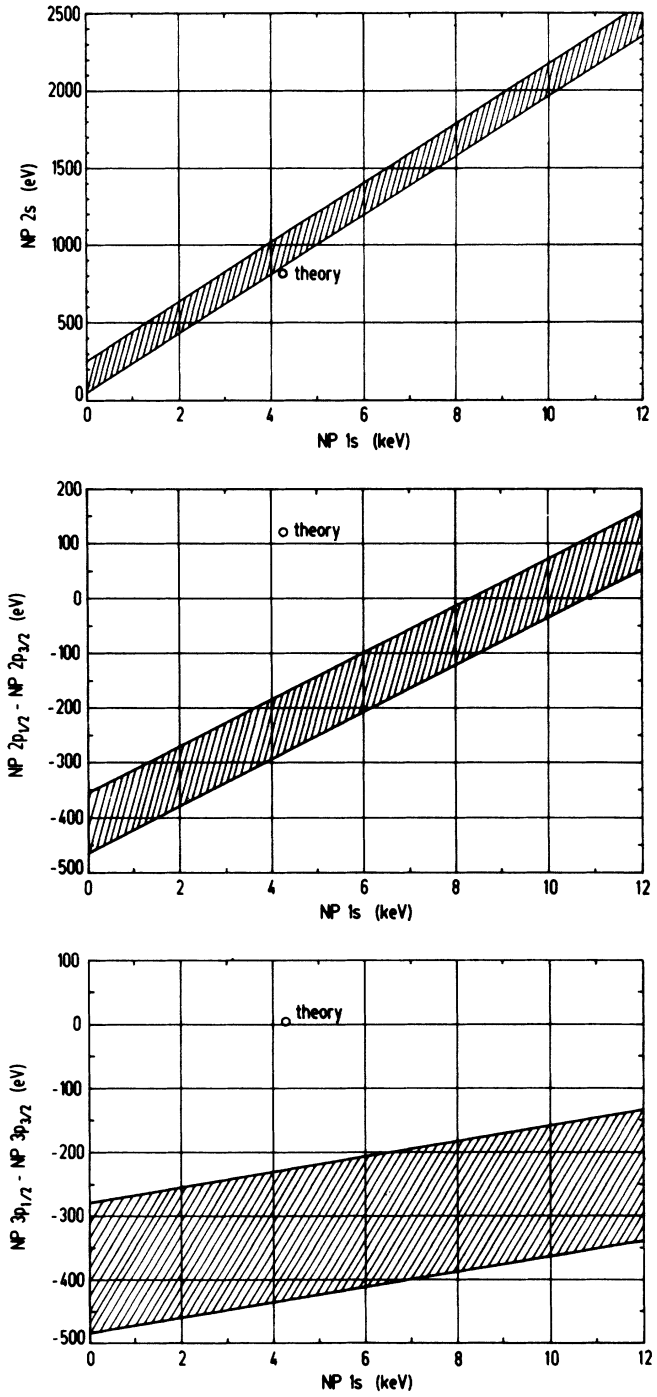

FIG. 4. Correlations between nuclear polarization corrections: (a) $C_{\mathrm{NP},2s}$ vs $C_{\mathrm{NP},1s}$. (b) Difference $\Delta C_{\mathrm{NP},2p}$ vs $C_{\mathrm{NP},1s}$. (c) Difference $\Delta C_{\mathrm{NP},3p}$ vs $C_{\mathrm{NP},1s}$. The shaded areas $\Delta C_{\mathrm{NP},3p}$ correspond to estimated experimental errors (see text).

D. Best fit NP values

Since the nine measured transition energies do not provide enough information for a simultaneous adjustment of more than six nuclear polarization or charge parameters, supplementary assumptions about at least four of these parameters have to be made.

Regarding the agreement between theoretical and experimental $1s$ and $2s$ NP shifts in the above correlation analysis, we have fixed the $C_{\mathrm{NP},1s}$ correction at its theoretical value for the following analysis. Such a choice is corroborated by the good agreement of the equivalent radii associated to the transitions involving the $1s$ state in the radial moment analysis of Sec. V B.

In addition, we have taken the relatively small NP values for the two $3d$ states from theory and fixed the diffuseness parameter a from elastic electron scattering data.[32] Hence, we are left with six free parameters to fit the experimental data, namely the half-density radius c, $C_{\mathrm{NP},2s}$, $C_{\mathrm{NP},2p_{1/2}}$, $C_{\mathrm{NP},2p_{3/2}}$, $C_{\mathrm{NP},3p_{1/2}}$, and $C_{\mathrm{NP},3p_{3/2}}$. The transition energies resulting from this fit are shown in column 5 of Table IX. The χ^2 value per degree of freedom is now 0.19, and the $2p$ as well as the $3p$ splittings are well reproduced. The fit demands larger NP values for the $p_{3/2}$ states than for the $p_{1/2}$ states, as already shown in the correlation analysis above. The NP corrections resulting from this fit are listed together with the theoretical ones in Table VIII. The quoted errors are taken from the correlation analysis of Sec. V C.

The above NP corrections and nuclear parameters, subsequently called "best-fit values," were checked in a series of other six-parameter fits, ensuring their stability against widely different start parameters in the input of the fitting routine. As an example, taking the $C_{\mathrm{NP},2p}$

TABLE VIII. Nuclear parameters determined from fits to the measured muonic transitions involving the 1s, 2s, 2p, and 3p levels in ^{208}Pb. The NP corrections are given in eV, the Fermi charge parameters in fm. Also included in the table are the rms radius (in fm), the calculated and experimental p splittings (in keV), and the χ^2 values per degree of freedom. The second column employs theoretical NP values. The third column results from the fit with c, $C_{NP,2s}$, both $C_{NP,2p}$ and both $C_{NP,3p}$ varied. The diffuseness parameter a is taken from electron scattering data.[32] The NP errors are mainly due to a ±4 am variation of this parameter, but also include a 30% error in $C_{NP,3d}$ besides the statistical fit errors.

Nuclear parameter	Fit with theoretical NP	Best fit values
c	6.644 7(5)	6.651 6(5)
a	0.524 9(3)	0.520 3
NP1s	4 252	4 252
NP2s	816	964(105)
NP2$p_{1/2}$	1 616	1 307(162)
NP2$p_{3/2}$	1 495	1 534(154)
NP3$p_{1/2}$	540	525(77)
NP3$p_{3/2}$	536	855(94)
NP3$d_{3/2}$	240	240
NP3$d_{5/2}$	45	45
rms radius	5.504 0(11)	5.503 1(11)
2p splitting calc.	185.112	184.776
2p splitting expt.	184.788(27)	184.788(27)
3p splitting calc.	47.531	47.196
3p splitting expt.	47.197(45)	47.197(45)
χ^2/DF	187.	0.19

values of the best fit and varying c, a, $C_{NP,1s}$ $C_{NP,2s}$, $C_{NP,3p_{1/2}}$, and $C_{NP,3p_{3/2}}$ reproduces the charge parameters c and a to within 0.1 am, while the NP values deviate by no more than 2 eV from the best-fit values.

In spite of the good internal consistency obtained by using the above best-fit NP values and the smallness of their errors, one cannot take the above procedure as an absolute measurement of nuclear polarization corrections. In fact the dynamical effects are interrelated with the static charge distribution. This especially concerns the NP corrections of the s states, since the predominant monopole excitations involving these states could also be reproduced by deflating the static charge distribution. Regarding the p states however, higher-order multipole excitations dominate in the NP shifts, rendering static and dynamical effects largely orthogonal.

Using the best-fit values, we again performed a radial moment analysis of the data. Such an analysis has already been described in Sec. V B. The results are summarized in Table IX and Fig. 3(b). In contrast to Fig. 3(a), there is now also excellent agreement for the 2p and 3p splittings.

The analysis of the muonic data alone yields a root-mean-square (rms) radius of $\langle r^2\rangle^{1/2}=5.5031(11)$ fm, in good agreement with the most recent elastic-electron scattering value[34] of 5.503(6) fm.

VI. CONCLUSION

Our experiment presents a complete set of muonic transition energies which are sensitive to the nuclear charge extension of ^{208}Pb. The precisions are generally five times higher than in former measurements. In particular, the 2p-1s transition energies can be employed as calibration values in future experiments with heavy muonic atoms.

Besides accurate nuclear charge moments, experimental correlations between the NP shifts of the lower muonic levels could be derived from fits to our measured data. They point to serious discrepancies in the differences of the NP corrections of the 2p and 3p levels. Whereas theory predicts larger NP corrections for the $p_{1/2}$ than for the $p_{3/2}$ levels, agreement between measured and calculated transition energies requires an inversion of the magnitude of the respective NP values. An alternative way to bring theory in accordance with experiment must admit values for $C_{NP,1s}$ larger than 12 or 31 keV, respectively. However, theoretical considerations as well as combined analyses of elastic scattering data (Ref. 8 and Sec. V C) reject such large values. Hence, the inversion in magnitude of the NP values of the p states has to be considered as an experimental fact. Since the same effect is observed in the 2p states and in the 3p states, accidental unobserved resonance excitations become highly unlikely. Our results reproduce the findings of a recent μ^--^{90}Zr experiment by our group[11] which shows the same discrepancy for the 2p splitting. In addition, we find effects of the same order of magnitude in both the 2p and 3p splittings, although the theoretical NP values are about three times smaller in the 3p than in the 2p levels. On the other hand, no discrepancy is seen for the 3d splitting.

Questioning other corrections besides the NP shifts which have to be applied to the muonic energy levels, one can exclude the first order vacuum polarization correction, which has been verified to the order of 0.1%.[3] The

TABLE IX. Calculated and experimental transition energies and their associated equivalent radii, using the best-fit NP values and nuclear parameters.

Transition	C_z (fm/eV)	k	Experimental energy E (keV)	Calculated energy E^0 (keV)	$E-E^0$ (eV)	Equivalent radii Calc. $R^0_{k,\alpha}$ [c] (fm)	Equivalent radii Expt. $R_{k,\alpha}$ [d] (fm)
$2s_{1/2}$-$2p_{1/2}$	−2.134−5	1.147 7	1 215.330(30)	1 215.324	6	6.880 9	6.880 8(6;16)
$2s_{1/2}$-$2p_{3/2}$	−1.266−5	1.401 4	1 030.543(27)	1 030.548	−5	5.940 4	6.940 5(3;23)
$3p_{1/2}$-$2s_{1/2}$	8.545−6	1.850 0	1 460.558(32)	1 460.558	0	6.996 6	6.996 6(3;9)
$3p_{3/2}$-$2s_{1/2}$	7.908−6	1.872 8	1 507.754(50)	1 507.754	0	6.998 8	6.998 8(4;10)
$2p_{1/2}$-$1s_{1/2}$	1.478−6	2.243 6	5 778.058(100)	5 778.069	−11	7.031 7	7.031 7(1;6)
$2p_{3/2}$-$1s_{1/2}$	1.407−6	2.256 2	5 962.854(90)	5 962.845	9	7.032 8	7.032 8(1;6)
$3p_{3/2}$-$1s_{1/2}$	1.313−6	2.339 4	8 501.151(110)[a]	8 501.148	3	7.039 5	7.039 5(1;6)
$3p_{1/2}$-$1s_{1/2}$	1.330−6	2.340 7	8 453.946(105)[a]	8 453.952	−6	7.039 6	7.039 6(1;6)
$3d_{5/2}$-$1s_{1/2}$	1.271−6	2.374 4	8 463.444(95)[a]	8 463.429	15	7.042 2	7.042 2(1;5)
$2s_{1/2}$-$1s_{1/2}$	1.573−6	2.461 1	6 993.393(100)[a]	6 993.393	0	7.049 0	7.049 0(2;7)
$\Delta(2p)$	2.922−5	2.532 1	184.788(27)[b]	184.776	12	7.054 4	7.054 8(8;47)
$\Delta(3p)$	1.045−4	3.234 5	47.197(45)[b]	47.196	1	7.105 2	7.105 2(47;145)
$3d_{3/2}$-$2p_{1/2}$	9.127−6	3.486 5	2 642.332(30)	2 642.339	−7	7.122 6	7.122 5(3;12)
$3d_{3/2}$-$2p_{3/2}$	1.332−5	4.000 5	2 457.569(70)	2 457.563	6	7.157 5	7.157 6(9;20)
$3d_{5/2}$-$2p_{3/2}$	1.314−5	4.007 5	2 500.590(30)	2 500.584	6	7.157 9	7.158 0(4;20)

[a]Derived from triangular sums of other measured transitions.
[b]Adopted mean value.
[c]Computed from best fit, $c=6.651\,614(470)$ fm, $a=0.520\,3(3)$ fm, $\alpha=0.141\,5$ fm^{-1}.
[d]$R_{k,\alpha}=R^0_{k,\alpha}+C_z(E-E^0)$, the first quoted error corresponds to the experimental error of the associated transition, the second error takes into account a 10% error on the NP corrections applied on the levels involved in the transition.

$2p$ levels would then, at most, be affected by 20 eV, and the $3p$ levels by 10 eV, whereas the NP discrepancies amount to 330 eV. Regarding higher-order vacuum polarization corrections, one would have to change these values by 50–100%, which seems to be a large overestimation with regard to a 20% precision in the experimental verification of these values.[20] Other, more exotic explications have been advanced by Rinker,[12] like anomalous spin- and isospin-dependent effects, but they are extremely unlikely.

In conclusion, there seems to exist a fundamental problem in present approaches to the calculation of the nuclear polarization effect. New theoretical and experimental efforts are necessary to clarify the situation in muonic atoms.

ACKNOWLEDGMENTS

The authors would like to thank T. Hennemann and Dr. G. Mallot for their valuable discussions and help regarding the elastic electron scattering data of ^{208}Pb. The authors thank F. Bienz and M. Boschung for their valuable help during the data-taking period. They are indebted to Dr. G. A. Rinker and Dr. Y. Tanaka for discussing the theoretical aspects of the nuclear polarization effects. For one of us (P.B.), this work was part of the requirements for his Ph.D. thesis. Finally, the authors would like to thank the Swiss National Foundation for financial support.

[1]J. A. Wheeler, Rev. Mod. Phys. **21**, 133 (1949).
[2]V. L. Fitch and J. Rainwater, Phys. Rev. **92**, 789 (1953).
[3]E. Borie and G. A. Rinker, Rev. Mod. Phys. **54**, 67 (1982).
[4]R. K. Cole, Phys. Rev. **177**, 164 (1969).
[5]M. Y. Chen, Phys. Rev. C **1**, 1167 (1970).
[6]H. F. Skardhamar, Nucl. Phys. **A151**, 154 (1970).
[7]G. A. Rinker and J. Speth, Nucl. Phys. **A306**, 360 (1978).
[8]Y. Yamazaki, H. D. Wohlfahrt, E. B. Shera, M. V. Hoehn, and R. M. Steffen, Phys. Rev. Lett. **42**, 1470 (1979).
[9]D. Kessler, H. Mes, A. C. Thompson, H. L. Anderson, M. S. Dixit, C. K. Hargrove, and R. J. McKee, Phys. Rev. C **11**, 1719 (1975).
[10]H. Euteneuer, J. Friedrich, and N. Voegler, Z. Phys. A **280**, 165 (1977); Nucl. Phys. **A298**, 452 (1978).
[11]T. Q. Phan, P. Bergem, A. Rüetschi, L. A. Schaller, and L. Schellenberg, Phys. Rev. C **32**, 609 (1985).
[12]G. A. Rinker, in Proceedings of the 15th LAMPF Users Group Meeting, Report LA-9260-C, Los Alamos, 1981.
[13]P. Bergem, M. Boschung, T. Q. Phan, G. Piller, A. Rüetschi, L. A. Schaller, L. Schellenberg, H. Schneuwly, M. V. Hoehn, and E. B. Shera, in Contributions to the 10th International Conference on Particles and Nuclei PANIC, Heidelberg, 1984, edited by F. Güttner, B. Povh and G. zu Putlitz (unpublished).
[14]P. Bergem, F. Bienz, M. Boschung, T. Q. Phan, G. Piller, A. Rüetschi, L. A. Schaller, L. Schellenberg, and H. Schneuwly,

Helv. Phys. Acta **60**, 736 (1987).
[15]L. A. Schaller, in Proceedings of the Symposium on Collective Phenomena in Nuclear and Subnuclear Interactions in Nuclei, Bad Honnef, BRD, 1987 (World-Scientific, Singapore, 1988, in press).
[16]G. A. Rinker and J. Speth, Nucl. Phys. **A306**, 397 (1978).
[17]M. J. Martin, Nucl. Data Sheets **47**, 797 (1986).
[18]G. A. Rinker, Comput. Phys. Commun. **16**, 221 (1979); Y. Tanaka, The Formalism of MUON2 and XRAY2, Los Alamos, 1984 (unpublished).
[19]P. Bergem, thesis, Institut de Physique, Université de Fribourg, 1982.
[20]T. Dubler, K. Kaeser, B. Robert-Tissot, L. A. Schaller, L. Schellenberg, and H. Schneuwly, Nucl. Phys. **A294**, 397 (1978).
[21]L. A. Schaller, L. Schellenberg, T. Q. Phan, G. Piller, A. Rüetschi, and H. Schneuwly, Nucl. Phys. **A379**, 523 (1982).
[22]A. Rüetschi, L. Schellenberg, T. Q. Phan, G. Piller, L. A. Schaller, and H. Schneuwly, Nucl. Phys. **A422**, 461 (1984).
[23]E. B. Shera, Phys. Rev. C **26**, 2321 (1982).
[24]T. J. Kennett, W. V. Prestwich, and J. S. Tsai, Nucl. Instrum. Methods **A247**, 420 (1986).
[25]R. G. Helmer, P. H. M. Van Assche, and C. Van der Leun, At. Data Nucl. Data Tables **24**, 39 (1979); R. G. Helmer, R. C. Greenwood, and R. J. Gehrke, Nucl. Instrum. Methods **155**, 189 (1978).
[26]G. Mallot (private communication).
[27]M. V. Hoehn and E. B. Shera, Phys. Rev. C **30**, 704 (1984).
[28]K. W. Ford and J. G. Wills, Phys. Rev. **185**, 1429 (1969).
[29]R. C. Barrett, Phys. Lett. **33B**, 388 (1970).
[30]M. Mallinger, thesis, Institut de Physique, Université de Fribourg, 1982.
[31]K. W. Ford and G. A. Rinker, Phys. Rev. C **7**, 1206 (1973).
[32]J. Friedrich and N. Voegler, Nucl. Phys. **A373**, 192 (1982).
[33]J. Friedrich (private communication).
[34]The analysis included (e,e) cross sections from Mainz, Stanford and Saclay. The Mainz data were normalized whereas normalization was left free on the other data.